DTU Library

Heat transfer and flow resistance analysis of a novel freeze-cast regenerator

Liang, Jierong; Deichmann Christiansen, Cathrine ; Engelbrecht, Kurt; Nielsen, Kaspar Kirstein; Bjørk, Rasmus; Bahl, Christian

Published in:
International Journal of Heat and Mass Transfer

Link to article, DOI:
10.1016/j.ijheatmasstransfer.2020.119772

Publication date:
2020

Document Version
Peer reviewed version

Citation (APA):
Liang, J., Deichmann Christiansen, C., Engelbrecht, K., Nielsen, K. K., Bjørk, R., & Bahl, C. (2020). Heat transfer and flow resistance analysis of a novel freeze-cast regenerator. *International Journal of Heat and Mass Transfer*, *155*, Article 119772. https://doi.org/10.1016/j.ijheatmasstransfer.2020.119772

Heat transfer and flow resistance analysis of a novel freeze-cast regenerator

Jierong Liang*, Cathrine D. Christiansen, Kurt Engelbrecht, Kaspar K. Nielsen, Rasmus Bjørk, Christian R.H. Bahl

Technical University of Denmark, Department of Energy Conversion and Storage, Anker Engelunds Vej, 2800 Kgs. Lyngby, Denmark

*E-mail address: jilia@dtu.dk

Abstract: The heat transfer and flow resistance of a novel freeze-cast porous regenerator of the magnetocaloric ceramic $La_{0.66}Ca_{0.27}Sr_{0.06}Mn_{1.05}O_3$ was experimentally characterized. Such a porous architecture may be useful as a regenerator geometry in magnetic refrigeration applications due to the sub-millimeter hydraulic diameters that can be achieved. Here the heat transfer effectiveness and friction losses are characterized using experiments and processed with a 1D numerical model. Empirical correlations of the friction factor and Nusselt number are reviewed and chosen for modelling the specific geometry. The experimental results show that the freeze-cast regenerator has increased heat transfer effectiveness and pressure drop compared to reference packed bed regenerators made from epoxy bonded spherical and irregular particles, as well as packed, unbonded spheres. Fixing the pressure drop and regenerator size, the freeze-cast regenerator achieves 10-15% higher heat transfer performance compared to packed bed regenerators.

Keywords：Magnetic regeneration; Thermal regenerator; Freeze-casting; Lamellar microchannel; Thermal evaluation

Nomenclature

Abbreviations		t^*	Phase angle, [-]
AMR	Active magnetic regenerator	U	Utilization, [-]
Gd	gadolinium	v	Velocity, [m/s]
LCSM	$La_{0.66}Ca_{0.27}Sr_{0.06}Mn_{1.05}O_3$	V	Volume, [m^3]
MCE	Magnetocaloric effect	S	Entropy, [J K^{-1}]
MCM	Magnetocaloric material	α	Specific surface area, [m^{-2}]
SEM	Scanning electron microscope	β_1-β_2	Correlation parameters, [-]
Variables		β	Scaling factor, [-]
A_c	Cross sectional area, [m^2]	σ	Standard deviation
c_1-c_4	Fitting parameters, [-]	Δ	Difference
c	Specific heat capacity, [J kg^{-1} K^{-1}]	ε	Porosity, [-]
D_h	Hydraulic diameter, [m]	η	Effectiveness, [-]
D_{sp}	Particle diameter, [m]	μ	Dynamic viscosity, [Pa·s]
f	Frequency, [Hz]	ρ	Density, [kg m^{-3}]
f_D	Darcy friction factor, [-]	τ	Period time, [s]
f_F	Fanning friction factor, [-]	$\mathfrak{T}$	Tortuosity, [-]
h	Convective heat transfer coefficient, [w m^{-2} K^{-1}]	**Subscripts**	
k	Thermal conductivity, [w m^{-1} K^{-1}]	c	Cold end
L	Length, [m]	disp	Dispersion
m	Mass, [kg]	f	Fluid
NTU	Number of transfer units, [-]	h	Hot end

Nu	Nusselt number, [-]	m	Macro
p	Pressure, [Pa]	Max	Maximum
Pe	Péclet number, [-]	Min	Minimum
Pr	Prandtl number, [-]	p	Pore
Re	Reynolds number	r	Regenerator
$\boldsymbol{r}$	Residual tensor, [-]	s	Solid
T	Temperature, [K]	stat	Static
t	Time, [s]	w	Wall

1. Introduction

1.1. Introduction to magnetic refrigeration

As one of the promising alternative refrigeration technologies, research in room temperature magnetic refrigeration mainly focusses on: magnetocaloric materials [1–3], magnet arrangements [4–6], and regenerator designs [7–9]. The last issue is to pursue the best practical performance of regenerators fabricated using industrially relevant magnetocaloric materials (MCMs) and processing paths. MCMs can convert energy from magnetic work (field change) to thermal energy (temperature change), based on the magnetocaloric effect [10]. Rare earths (gadolinium and its alloys) [11], intermetallics (La-Fe-Si based) [12] and ceramics (i.e. $La_{0.66}Ca_{0.33-x}Sr_xMn_{1.05}O_3$) [13] are commonly used MCMs for the applications of room temperature magnetic refrigeration. Due to the intrinsic material characteristics, the magnetocaloric effect (MCE), except the giant MCE in the vicinity of the Curie temperature for some MCMs [14], is normally small [15,16]. The MCE is characterized by the isothermal entropy difference (ΔS_{iso}) and adiabatic temperature change (ΔT_{ad}). For the benchmark MCM gadolinium (Gd), the value of ΔT_{ad} in a 1 T magnetic field is about 3.0 - 3.5 K experimentally, depending on the purity of the Gd [17,18]. Thermodynamic cycles without regeneration configuration are restricted by the small ΔT_{ad}. The active magnetic regenerative cycle is generally adopted in magnetic refrigeration prototypes [19], which are based on progressively creating and maintaining an axial temperature gradient along the MCM regenerator [20]. The thermodynamic cycle for the active magnetic regenerator (AMR), for example the Brayton cycle, consists of four steps: 1) adiabatic magnetization; 2) iso-field flow from cold to hot reservoir through the regenerator; 3) adiabatic demagnetization; and 4) iso-field reverse flow. Each infinitesimally small part of the regenerator bed undergoes a unique refrigeration cycle and interacts with the adjacent material via the heat transfer fluid.

The AMR characterization involves both the magnetocaloric and heat transfer properties of the regenerator, which are generally characterized based by the temperature span, cooling capacity and efficiency of the AMR system [21]. Other AMR studies have focused on flow profiles [22–25] and working conditions [26,27]. Potential regenerator geometries can be tested with an applied magnetic field as an active regenerator or with no applied magnetic field as a passive regenerator and various test devices of each type have been presented in the literature [28,29]. A passive testing device is essentially a synchronized AMR device with zero applied magnetic field. Passive testing focusses on the heat transfer performance and pressure drop characteristics of the geometry and can be performed on materials with or without a magnetocaloric effect. The effectiveness (η) and friction factor are the most important performance metrics that reflect the behavior of heat transfer and viscous friction. Lei et al. [30] compared effectiveness and friction factor between two epoxy bonded regenerators with spherical and irregular particles on a passive test rig. Trevizoli et al. [31] performed a parametric η-*NTU* analysis and viscous friction factor characterization of packed bed regenerators to be used in AMR cycles with different diameters of stainless steel spheres using a passive apparatus. Šarlah et al. [32] carried out passive experiments to characterize the Colburn *j*-factor and the friction factor among six different geometries. Passive characterization is an efficient way to focus on the behavior of heat and mass transfer, especially for a new regenerator morphology while ignoring the magnetocaloric effect.

In passive mode, the regenerator serves as a thermal storage heat exchanger with oscillating fluid flow. Intermittent alternating heat transfer takes place between the solid matrix and the fluid in two periods: 1) hot blow: fluid from the high-temperature reservoir warms up the solid matrix; 2) cold blow: reversing the fluid flow and the matrix releases the stored heat. From this point of view, an efficient regenerator requires [33]: 1) a large value of the overall heat transfer coefficient times surface area; 2) a large thermal inertia to decrease oscillations of interstitial temperature difference; and 3) a low friction factor to minimize pumping power consumption and viscous losses. Over the last decades, various geometries have been developed and tested for AMR applications, such as: 1) packed particle bed [34], 2) parallel plate [35], 3) micro-channel [36], and 4) packed screen bed [37]. These geometries have their own advantages and weaknesses. Concerning the heat transfer performance and friction dissipation, the parallel plates and micro-channel matrices normally exhibit small values [38,39]; while packed particle beds exhibit both high values of effectiveness and friction factor. Thus, any new geometry of regenerator might exhibit different heat transfer performance and parasitic losses, and needs to be passively characterized prior to being used in an AMR device. A new applicable geometry could be that of a freeze-cast ceramic.

1.2. Shaping by freeze-casting

Freeze-casting, or ice-templating, is a processing technique used to shape, typically, ceramics into monolithic, anisotropic structures with an aligned channel-geometry of highly tunable dimensions and porosity. The channels are typically on the order of ~1 to ~100 μm wide [40–42]. Freeze-cast structures have great mechanical durability and have been used in a broad range of applications, primarily within biomaterials for tissue engineering or membranes for catalysis, electrodes, filters etc. [43].

In freeze-casting, a suspension of ceramic particles in water is frozen directionally by bringing only one side of the suspension into contact with a cooling source. This initiates directional growth of ice crystals along the temperature gradient, causing a segregation of particles resulting in a two-phase structure of ceramic and ice. The latter is then removed by sublimation. Subsequent sintering results in a rigid ceramic structure with directional porosity in the form of parallel, well-defined channels as seen in Fig. 1a. The morphology and dimensions of these channels strongly depend on freezing conditions [41,44,45], while the porosity depends on the ceramic load of the slurry. The structural and dimensional characteristics, and thus flow properties of the freeze-cast structure, can thus be adjusted and optimized by changing processing parameters.

Utilizing this processing route for shaping of MCMs thus results in an attractive regenerator geometry of lamellar micro-channels as shown in Fig. 1. The MCM $La_{0.66,396}Ca_{0.27}Sr_{0.06}Mn_{1.05}O_3$ (LCSM) was primarily chosen for its low cost and its low reactivity with solvent. The freeze-cast geometry can be summarized as follows:

(1) Narrow, lamellar pores with an ellipsoid cross-section on the micrometer-scale. The lack of square corners for this pore shape, compared to other micro-channel geometries, could result in the increment in local heat transfer coefficient [46,47].
(2) Non-ordered orientations of the major axes of the ellipsoidal channels in the plane perpendicular to the flow direction.
(3) Low tortuosity, i.e. almost straight channels.
(4) Tunable porosity and large specific surface area, providing a geometry that will presumably exhibit high convection coefficient with reasonable flow resistance.

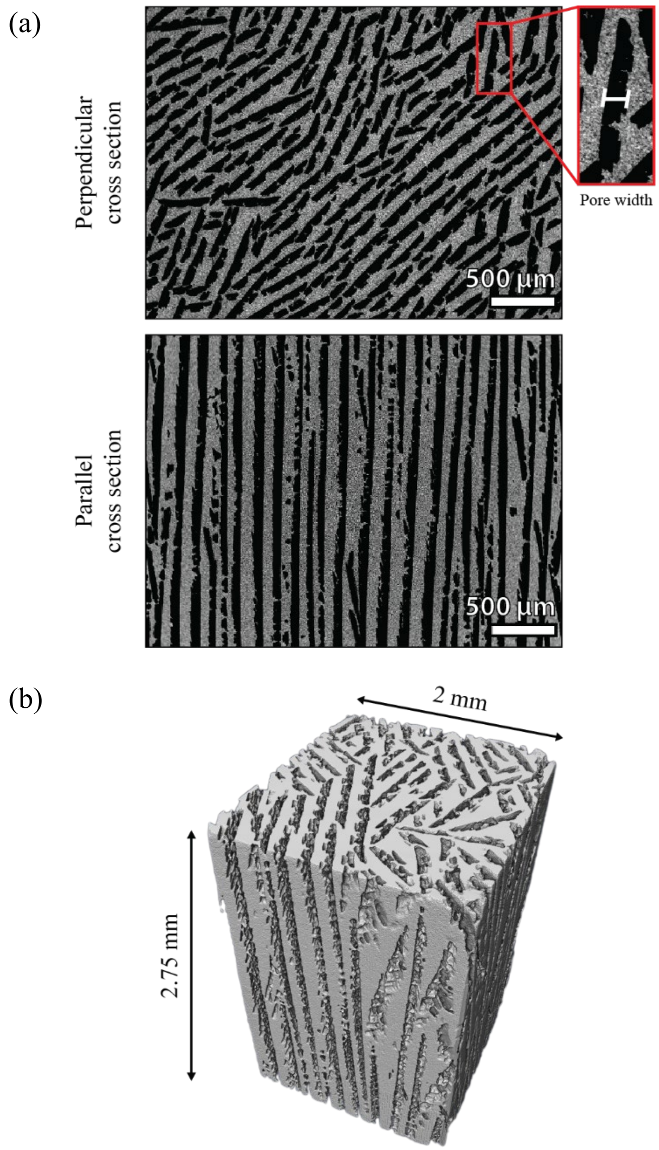

Fig. 1 Geometry of freeze-cast LCSM ceramics. (a) SEM micrographs of cross sections of a freeze-cast sample where grey areas are the ceramic walls and black areas are porosity in the form of aligned, lamellar channels. Micrographs are obtained at cross sections perpendicular and parallel to the freezing direction in the center of the structure. (b) 3D reconstruction of freeze-cast LCSM specimen segment based on interactive segmentation using Avizo software (Thermo Fischer Scientific) of tomography images obtained using an X-ray Microscope (ZEISS Xradia 520 Versa).

In this paper, we propose a novel freeze-cast matrix as a possible regenerator for an AMR and present measurements of regenerator effectiveness and pressure drop for a freeze-cast regenerator. These results are compared with a packed bed of spheres, which is considered a baseline AMR regenerator geometry. Furthermore, a 1D model framework [48] is used to derive the specific empirical correlations of Nusselt number and friction factor by fitting the model to the measured inlet and outlet temperatures and measured pressure drops. The numerical model is validated over a broad range of operating conditions. The model helps to better understand the internal phenomena of heat transfer and flow resistance, which is difficult to measure experimentally. The thermal evaluations can be used to assist in the new regenerator development of physics-based predictive capabilities, performance metrics, and design guidelines.

2. Sample fabrication and characterization

2.1. Freeze-casting procedure

The fabrication and characterization of freeze-cast ceramics follows the process described by Christiansen *et al.* [45,49], with slight alterations regarding suspension composition and freezing conditions.

Freeze-cast ceramics were prepared from suspensions of 30 vol% of LCSM (CerPoTech, Norway) in MiliQ water with 2.5 wt%, solid to ceramic ratio, of dispersant (DURAMAX™ D-3005, Rohm and Haas, Dow Chemical, USA). Additionally, the pH of the suspension was adjusted from ~8 to ~6.5 with dropwise addition of 1 molar nitric acid to establish a sufficient dispersion of particles, where the final pH was verified using a pH-meter (780, Metrohm). The suspension was then mixed on a low energy ball mill with alumina balls (Ø10 mm) for at least 72 hours until a consistent particle size of d_{50} = 1.2 µm was reached. 2 wt%, solid to ceramic ratio, of binder (DURAMAX™ B-1022, Rohm and Haas, Dow Chemical, USA) was added and the suspension was mixed for an additional 24 hours. Both binder and dispersing agent were chosen based on their low viscosity and thus suspensions were easily de-aired immediately before casting by brief sonication in order to avoid bubbles.

Cylindrical Teflon™ molds, with inner diameter of 30.5 mm and outer diameter of 50 mm, and a detachable copper bottom were pre-cooled in an ice-bath along with the ceramic suspension prior to casting. The suspension was poured into the mold, which was then attached to the cold finger of a novel freeze-casting device utilizing thermoelectric cooling for precise temperature control, making it possible to set a specific temperature profile of the cold finger during casting. By lowering the temperature of the cold finger while keeping the suspension and mold open to ambient conditions of 5 °C, the suspension is frozen directionally from the bottom and up. The temperature of the cold finger is kept at 2.5°C for 300 s prior to freezing to equilibrate the temperature of the mold and suspension, and is then decreased at -1 K/min until the entire suspension is frozen solid. A linearly decreasing temperature profile was chosen in order to achieve homogenous channel widths along the sample height in accordance with previous work [45].

Ice was subsequently removed from the frozen samples in a freeze-drier (Christ Alpha 1-2 LD plus, Buch & Holm) for 24 hours. Dry samples were fired in air, initially burning out the organic additives at 250 and 450 °C, with a holdtime of 2 hours at each temperature and a heating rate of 15 K/min, followed by sintering at 1100 °C for 12 hours with a heating rate of 30 K/min.

2.1.1. Structural characterization of freeze-cast ceramics

Freeze-cast samples for testing were cut into smaller pieces as described in section 2.1.2. Top and bottom parts were mounted in epoxy (Epofix, Struers, Denmark), and the cross section was then imaged using a scanning electron microscope (TM3000, Hitachi High-Technologies). The analysis of micrographs follows that described by Christiansen *et al*. [45], where channel width (as defined in Fig. 1a), macro porosity and tortuosity are determined. Additionally, the perimeter of channels can be measured in binarized micrographs of cross sections perpendicular to the freezing direction yielding a measurement of the specific surface area. A total of 21 micrographs, each covering ~300 channels in the perpendicular cross section, obtained evenly distributed across the cross sections of the freeze-cast samples have been analyzed to calculate the average structural parameters. These parameters have been summarized in Table 1. As measurements of the tortuosity requires imaging of cross sections parallel to the channel direction, and thus requires additional destructive procedures, the calculation of tortuosity is based on a sample fabricated from the same suspension and frozen under the same conditions.

As is seen on Fig. 1, the overall geometry of the channels in freeze-cast structures are lamellar with channels running along the freezing direction. In the horizontal plane the shape of channels are ellipsoidal with a pore width as shown on Fig. 1. While the orientation of channels in the horizontal plane is ordered in smaller domains, channels are highly aligned in the plane parallel to the freezing direction. Tortuosity is a measure of this alignment and curviness of channels and is calculated as the ratio between the direct distance across a cross section parallel to the freezing direction and the average distance through a channel. Thus, a tortuosity of $\mathfrak{T} = 1$ describes a direct flow path through the structure, while an increase in tortuosity corresponds to an increasingly curved and obstructed flow path.

The total porosity, or sample porosity, ε, of ~70 % of the freeze-cast structure is directly related to the ceramic load of the suspension during processing. To omit non-desired distorted channels at the two ends of the specimen, only two thirds of this in length is accounted for by channels in the final structure, i.e. the channel porosity or macro porosity, ε_{p}, as given in Table 1. The remaining porosity consists of micro porosity in the walls. As only the macro porosity is assumed to act as flow paths for fluid, ε_{p} is used for determining pore velocity while ε is adopted for solid mass calculations. Additionally, the hydraulic diameter is derived as follows:

$$D_h = 4\varepsilon_m/\alpha \qquad (1)$$

where α is the specific surface area. The specific area α is determined by the sum of total cross sectional perimeter of each channel per area from image analysis, i.e. the cross sectional view in Fig. 1 (a) and ignores the small protrusions that can be seen in some channels.

2.1.2. Preparation of freeze-cast regenerator

A single freeze-cast regenerator matrix is composed of two combined monolithic pieces of freeze-cast ceramic frozen at identical conditions and thus with homogenous structural characteristics. Two pieces are used to ensure a sufficient length and thermal mass of the regenerator for the AMR system used. Each piece of 15 mm is cut from a full freeze-cast sample with a length of approximately 29 mm. Due to the nature of freeze-cast ceramics, the bottom part of the sample does not contain aligned channels [50,51] and thus the bottom 8 mm and remaining top of the sample are discarded. The matrix, with a total of 30.0 g, is mounted in a transparent housing (Ø30 mm × 40 mm) using silicone glue, sealing possible gaps between the housing and the solid matrix and thus avoiding fluid flowing around the freeze-cast matrix. The transparent housing helps to observe the conditions of bypass flow and residual bubbles.

2.2. Reference regenerators

Three benchmark regenerators were used for comparison. One is a Gd packed sphere bed regenerator which is used as baseline and tested in this study, as this is the most commonly used type of regenerator for passive and active characterizations in magnetic refrigeration. Furthermore, epoxy bonded regenerators made from irregular or spherical particles of $La(Fe,Mn,Si)_{13}H_y$ referred to as VAC-A and VAC-B, respectively, are used as a mean of testing state of the art magnetocaloric regenerators.

The diameter of particles in the Gd bed is ~0.3 mm, and it uses the same housing as the freeze-cast regenerator. A mesh screen is used to keep the particles in the housing. Although this housing geometry is not optimal for the Gd regenerator, it is important to ensure that the tested regenerators have the same system effects beyond the regenerator, such as dead volume loss and heat leaks. The end views of the freeze-cast and packed bed regenerators are shown in Fig. 2.

(a) (b)

Fig. 2 End views of (a) freeze-cast regenerator and (b) packed bed regenerator.

The epoxy bonded regenerators were not tested in this work. Instead their experimental data are taken from the references [30,48] directly. Note that the epoxy bonded regenerators are loaded in the same tester but with a smaller housing diameter, which results in a smaller dead volume. Thus, the effectiveness measure of the epoxy bonded regenerators would not suffer from additional losses caused by the dead volume effect compared to the freeze-cast regenerator. On the other hand, the pressure drop measure between all these regenerators can be assumed as a fair comparison due to the same sensors and tubing. The geometry parameters of the reference regenerators in this paper are included in Table 1.

Table 1: Geometry parameters of tested regenerators. Structural characteristics of freeze-cast ceramics are from image analysis of obtained micrographs. The corresponding measurements are based on the analysis of 15 images evenly distributed along the height parallel to the freezing direction of a freeze-cast sample and are given as an average. Data of other reference regenerators are also introduced from the publish works. The size of housing is specified as diameter and length.

Parameters	Freeze-cast	Gd packed bed [48]	VAC-A [30]	VAC-B [30]
Housing (mm×mm)	Ø30×40	Ø30×40	Ø20×70	Ø20×70
Pore width (μm)	72.0 ± 6.4	/	/	/
Avg. particle diameter (mm)	/	0.3	0.56	0.58
Sample porosity	0.72	0.45	0.46	0.48
Macro porosity	0.42	0.45	0.46	0.48
Hydraulic diameter (mm)	0.102	0.160	0.410	0.380
Specific surface area (m^{-1})	1.64×10^4	1.10×10^4	4.49×10^3	5.05×10^3
Tortuosity	1.6 ± 0.3	/	/	/

3. Passive characterization of heat transfer and pressure drop

3.1. Experimental setup description

The infrastructure of the passive regenerator test apparatus was published previously [30]. The instrumentation and connections are shown in Fig. 3, including the regenerator assembly, cold and hot reservoirs, piston and motor assembly and check valves.

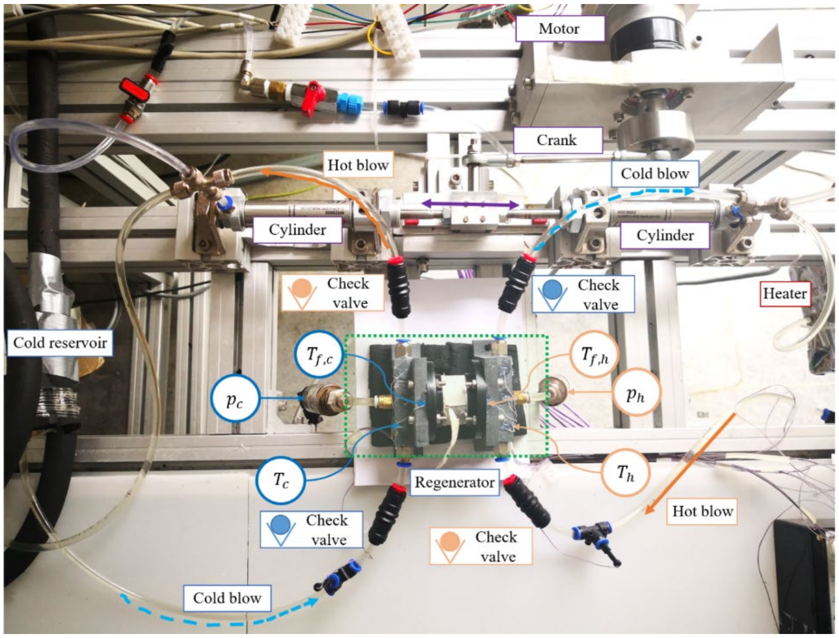

(a)

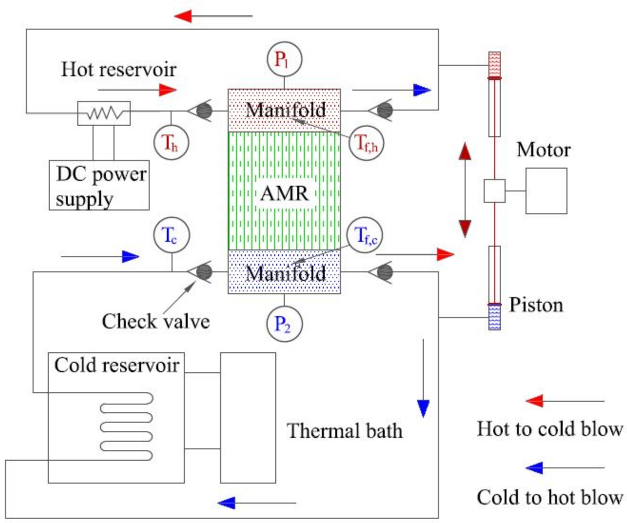

(b)

Fig. 3 (a) Passive test rig with hot blow and cold blow flow directions illustrated. (b) Schematic of the regenerator connected to manifolds at both ends. Each manifold integrates the functions of flow separation, thermocouple and pressure transducer installations. The outflow from the manifold will go through the outlet check valve, piston, cold reservoir or heater, inlet check valve, and then back to the inlet of the manifold.

The regenerator assembly consists of regenerative material, 3D-printed resin housing and manifolds with thermocouples (Omega, type E) and pressure transducers (Gems, 2.5 bar). Within the green dashed box shown in Fig. 3, four check valves direct the fluid flow. The end temperature probes are set in $T_{\mathrm{f,h}}$ and $T_{\mathrm{f,c}}$, which are positioned to almost touch the screens at each end of the regenerator. Another two thermocouples that represent inflow and outflow temperatures, are positioned in T_{h} and T_{c} outside the dashed box. Two pressure transducers are set at the ends of the regenerators measuring the pressure drop. Data acquisition is performed with a National Instruments (NI) cDAQ9174 system connected to an NI 9213 thermocouple module and an NI 9203 current module (for the pressure transducers). The tests are performed using tap water as the heat transfer fluid.

The piston and motor assembly is a motor-crank system connected to two cylinders, one for each direction of flow. The motor rotary frequency control and displacement record are implemented by a linear encoder. The oscillating flow is generated by the reciprocating movement of the two cylinders. In Fig. 3, the solid arrows represent the hot blow, while the dashed arrows indicate the cold blow.

All tests performed in this work are carried out for balanced flow conditions in both the freeze-cast regenerator and the Gd packed sphere bed regenerator. The temperature span between the hot and cold end is set as a constant for comparison. With a small temperature span it is not easy to capture the temperature breakthroughs in $T_{f,h}$ and $T_{f,c}$ during the blow, and therefore a 10 K span is used here, as this is suitable based on the existing heater capacity. To reveal the heat capacity sensitivity on local temperature and bound the Curie temperature of LCSM (~19℃,), the variation of cold reservoir temperature T_c tested is from 15 ℃ to 30 ℃, with an increment of 5 ℃. Four testing temperature intervals are selected considering the effect of the local specific heat variation of LSCM. In Fig. 4, the four intervals indicate the different trends of specific heat, which represent the peak bounded, decreasing region, buffer region and flat region, respectively. During each measurement with fixed reservoir temperatures, the piston stroke was adjusted to control the thermal mass of the fluid, in order to keep the utilization constant. The frequency was varied from 0.50 to 2 Hz in steps of 0.25 Hz. The uncertainty analysis is described in Appendix. A.

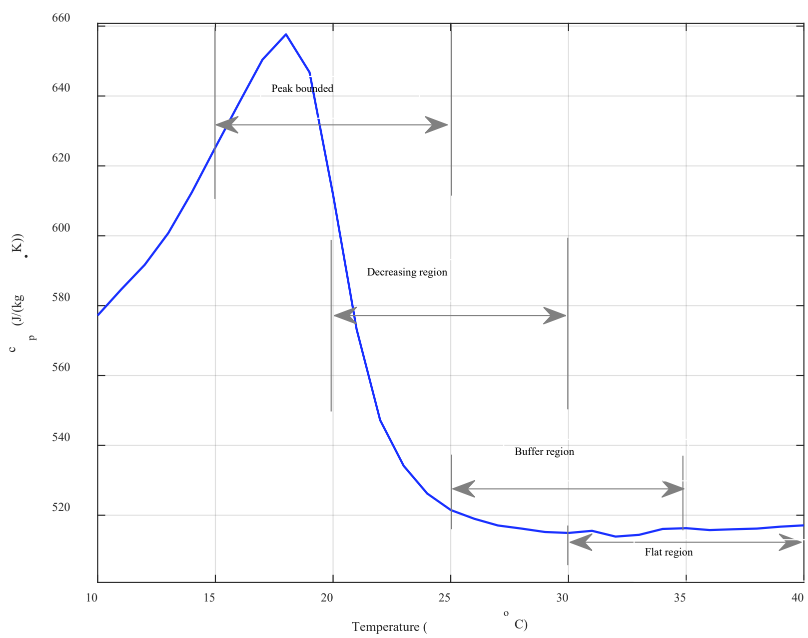

Fig. 4 Temperature dependency of specific heat capacity of LCSM in zero field.

3.1.1.Performance metrics

To introduce the effectiveness-NTU method for passive characterization, the relationship of effectiveness, utilization (U) and number of transfer unit (NTU) will be investigated experimentally and numerically in the following section. The utilization is a preliminary design parameter to characterize the system configuration [28]. Due to small-scale channels, in the expression for the U we assume that the solid thermal mass accounts for the total thermal mass, the fluid specific heat capacity is temperature independent and the flows are balanced.

$$U = \frac{\int_0^{\tau/2} \dot{m}_f c_f dt}{m_s c_s} \quad (2)$$

Here the subscripts f and s denote solid and fluid respectively. Throughout this paper, periods from 0 to $\tau/2$ and from $\tau/2$ to τ indicates the hot to cold blow and the cold to hot blow, respectively. Note that the background value of the solid specific heat capacity c_s= 518 J·kg^{-1}·K^{-1} is used rather than the peak value. As a measure of the intensity of heat transfer, the NTU is defined as:

$$NTU = \frac{h\alpha V_r}{2/\tau \int_{\tau/2}^{\tau} \dot{m}_{f,c} c_{f,c}\, dt} \quad (3)$$

where h, α and V_r are heat transfer coefficient, specific surface area and regenerator volume, respectively. $\dot{m}_{f,c} c_{f,c}$ indicates that the thermal mass rate is taken from the cold blow. Accordingly, the Nu is defined as:

$$Nu = \frac{hD_h}{k_f} \quad (4)$$

where D_h and k_f are hydraulic diameter and thermal conductivity of the fluid. As a metric of heat transfer performance, the effectiveness in each blow period (subscripts h and c are for hot and cold blow, respectively) are given by:

$$\eta_h = \frac{T_h - 2/\tau \int_{\tau/2}^{\tau} T_{f,c}\, dt}{T_h - T_c} \quad (5)$$

$$\eta_c = \frac{2/\tau \int_0^{\tau/2} T_{f,h}\, dt - T_c}{T_h - T_c} \quad (6)$$

Flow resistance is characterized by the relationship between the Fanning friction factor (f_F) and Reynolds number (Re). In oscillatory flow situations, pressure drop amplitude and cycle average pressure drop are adopted to define the oscillatory friction factor (f_{osc}) [52] and cycle average friction factor (f_{avg}) [53] respectively. f_{osc} is suitable for correlation fitting, flow pattern and system operating range determinations [54,55], while f_{avg} is directly linked to pumping work and comparison with steady flow [56]. To be consistent with the existing framework of f_F correlations in Table B1 which will be discussed below, f_{osc} is selected to define the friction factor.

$$f_F = \frac{\Delta p_{max}}{L_r} \frac{D_h}{2\rho_f \left(v_{f,max}\right)^2} \quad (7)$$

Regarding the definition of Re, the velocity term can be superficial velocity, pore velocity or angular velocity. Here the Reynolds number based on the pore velocity is chosen also to be consistent with the correlations in Table B1:

$$Re_p = \frac{\rho_f (v_{f,max}/\varepsilon_p) D_h}{\mu_f} \quad (8)$$

where v_f and μ_f are fluid superficial velocity and dynamic viscosity, respectively.

3.2. Data analysis tools

As a novel micro-channel matrix, there has been little research effort to model the solid-fluid heat transfer and flow resistance in freeze-cast sample like architectures. Developing the specific correlations for heat transfer and friction dissipation to be used in porous media models, is therefore necessary to derive the internal parameters i.e. Nu and NTU. It is also an effective tool for model predictions in the future.

3.2.1.Numerical model

Since a freeze-cast regenerator as a random geometry cannot be fully addressed in a two-dimensional space, a 1D model is suitable here. The energy and mass governing equations are taken from Lei 2016 [48] to characterize the interior transient temperature distribution, as well as the pressure drop. The two equations are coupled by means of the heat convection term.

The energy balance on the fluid:

$$\underbrace{\frac{\partial}{\partial x}\left(k_{disp}A_c\frac{\partial T_f}{\partial x}\right)}_{\text{Heat conduction}} - \underbrace{\dot{m}_f\frac{\partial h_f}{\partial x}}_{\text{Enthalpy flow}} - \underbrace{\frac{Nuk_{disp}}{D_h}a_sA_c\left(T_f - T_s\right)}_{\text{Heat convection with solid}} - \underbrace{h_{w,f}a_{w,f}A_c\left(T_f - T_w\right)}_{\text{Heat convection with housing}} + \underbrace{\left|\frac{\partial p}{\partial x}\frac{\dot{m}_f}{\rho_f}\right|}_{\text{Viscous dissipation}} = \underbrace{A_c\varepsilon\rho_fc_f\frac{\partial T_f}{\partial t}}_{\text{Thermal storage rate}} \quad (9)$$

The solid energy equation:

$$\underbrace{\frac{\partial}{\partial x}\left(k_{stat}A_c\frac{\partial T_s}{\partial x}\right)}_{\text{Heat conduction}} + \underbrace{\frac{Nuk_{disp}}{D_h}a_sA_c\left(T_f - T_s\right)}_{\text{Heat convection}} = \underbrace{A_c(1-\varepsilon)\rho_sc_s\frac{\partial T_s}{\partial t}}_{\text{Thermal storage rate}} \quad (10)$$

where T, p, A_c, $\dot{m}$, h, ρ, c, ε, a and D_h are temperature, pressure, cross sectional area, mass flowrate, specific enthalpy, density, specific heat, sample porosity, specific area and hydraulic diameter, respectively. Subscripts f, s and w refer to fluid, solid and housing wall, respectively. The static conductivity (k_{stat}) and fluid dispersion (k_{disp}) conductivity, which are considering the 3-D conduction and axial dispersion effect in porous AMR beds, respectively, are illustrated in Eq. (11-12) [57].

$$k_{stat} = (1-\varepsilon)k_s + \varepsilon k_f \quad (11)$$

$$k_{disp} = k_f\frac{Pe^2}{210} \quad (12)$$

where Pe is the Péclet number. This 1D model integrates all the major terms of (1) temperature dependence of fluid properties (dynamic link to CoolProp [58]), interpolation from experimental data in magnetocaloric effect and demagnetization factor [59], (3) temperature dependent heat capacity of MCM, (4) axial thermal conduction, (5) pressure drop and (6) thermal dispersion.

3.2.2.Form of Nusselt number and friction factor correlations

The specific correlations can be derived from the existing correlations of laminar flow with micro-channels in Table 2. These correlations typically show a difference between the flow conditions of steady state or oscillatory flow, the region of developing or developed flow, and different channel shapes. The following correlation forms are chosen considering the flow characteristics of developing and oscillatory within the narrow shape micro-channels and use the same form as [60] for the friction factor and Nu:

$$f_{\text{F}} = c_1Re_p^{-1} + c_2 \quad (13)$$

$$Nu = c_3\left[L_r/\left(D_hRe_pPr\right)\right]^{c_4} \quad (14)$$

where $c_1 \sim c_4$ are fitting parameters that are assumed to depend on the matrix geometry. Since only average geometrical parameters are available in this study, parameters c_1 - c_4 are fitted by averaging. This implies that the geometrical parameters and therefore fitting parameters are spatially and temporally uniform. Only operating conditions, such as temperatures and velocities, cause the variations of local f_{F} and Nu. Note that the correlations are valid for liquid laminar flow.

$$[c_1, c_2, c_3, c_4] = \boldsymbol{f}(D_h, \mathfrak{T}) \quad (15)$$

$\mathfrak{T}$ is the channel tortuosity:

$$\mathfrak{T} = L_p / L_r \quad (16)$$

where L_{p} is the average length of geometrical flow path of pores, L_{r} is the straight-line length of the regenerator sample. When one specific matrix is designated, the parameters of $c_1 \sim c_4$ can be treated as constants and fitted from experimental results.

Table 2: Correlations for the average Nusselt number and friction factor in micro-channels matrix. The Reynolds number in the table is based on the pore velocity. Heat transfer fluid is assumed to be incompressible

References	Boundary condition	Correlations	Fitting form
Shih [61]	Developed laminar flow, rectangular	$f_F = 24(1 - 1.3553 \propto + 1.9467 \propto^2 - 1.7012 \propto^3 + 0.9564 \propto^4 - 0.2537 \propto^5)/Re$, $\propto$ is aspect ratio.	$f_F = P(\propto)/Re$ P is a polynomial function.
Jiang et al. [60]	Developed laminar flow, rectangular	$f_D = 68.53/Re$, smooth. $f_D = 1639/Re^{1.48}$, $Re < 600$, roughness. $f_D = 36.4/Re + 0.45$, porous. f_D is the Darcy friction factor, which is four times of the Fanning friction factor: $f_D = 4f_F$.	$f_D = aRe^b + c$
Hornbeck [62]	Developing laminar flow, circular	$f_{app} = \frac{D_h}{4L}(13.74(x^+)^{1/2} + (1.25 + 64x^+ - 13.74(x^+)^{1/2})/(1 + 0.0021(x^+)^{-2}))$, f_{app} is apparent friction factor. x^+ is non-dimensionalized length: $x^+ = L_r/\left(D_h Re_p\right)$	As left
Steink and Kandlikar [63]	Developing laminar flow, rectangular	$K(\infty) = 0.6796 + 1.2197 \propto + 3.3089 \propto^2 - 9.5921 \propto^3 + 8.9089 \propto^4 - 2.9959 \propto^5$, $K(\infty)$ is Hagenbach's factor.	$f_{app} = f + \frac{D_h}{4x}P(\propto)$
Lorenzini and Morini [64]	Developed laminar flow, trapezoidal and rectangular with rounded corners	For each fixed $\propto$, $f_F = 14.226Re^{-1}\sum_{i=0}^{5} A_i\left(\frac{R_c}{H_{r1}}\right)^i$, $Nu = 3.608\sum_{i=0}^{5} A_i\left(\frac{R_c}{H_{r1}}\right)^i$. R_c is the curvature of the channel corner. H_{r1} is the height of a trapezoid or rectangle.	$f_F = P(\frac{R_c}{H_{r1}})\, Re^b$ $Nu = P(\frac{R_c}{H_{r1}})$
Liou et al. [65]	Laminar, parallelogram serpentine	$f_F = Re^{-0.8}\sum_{j=0}^{5}\sum_{i=0}^{5} A_{i,j} \propto^i \theta^j$ $Nu = Re^{0.5}\sum_{j=0}^{5}\sum_{i=0}^{5} B_{i,j} \propto^i \theta^j$ θ is included angle	$f = P(\propto, \theta)\, Re^a$ $Re = P(\propto, \theta)Re^b$
Choi et al. [66]	Laminar, circular	$Nu = 0.000972Re^{1.17}Pr^{1/3}$ $Re < 2000$	$Nu = aRe^bPr^c$
Hausen et al. [67]	Laminar, circular	$Nu = \frac{3.657 + 0.19(x^*)^{-0.8}}{1 + 0.117(x^*)^{-4.67}}$, x^* is dimensionless length: $x^* = L_r/\left(D_h Re_p Pr\right)$.	$Nu = \frac{a + b(x^*)^d}{1 + c(x^*)^e}$

Jiang et al. [60]	Laminar, rectangular	$Nu = 0.52(x^*)^{-0.62}$, $x^* < 0.05$. $Nu = 2.02(x^*)^{-0.31}$, $x^* > 0.05$.	$Nu = a(x^*)^b$
Kandlikar et al.[47]	Developed laminar flow, rectangular	$Nu = 8.235(1 - 10.6044 \propto +61.1755 \propto^2 - 155.1803 \propto^3 + 176.9203 \propto^4 - 72.9236 \propto^5)$	$Nu = P(\propto)$
Sadeghi et al. [68]	Developed laminar flow, arbitrary cross section	Characteristic length: $\sqrt{A}$ instead of D_h. $Nu_{\sqrt{A}} = C_1\left(\frac{I_p}{A^2}\right)^{C_2}\left(\frac{\sqrt{A}}{P}\right)^{C_3}$, I_p is polar moment of inertia, P is perimeter, A is cross sectional area.	$Nu_{\sqrt{A}} = C_1\left(\frac{I_p}{A^2}\right)^{C_2}\left(\frac{\sqrt{A}}{P}\right)^{C_3}$
Shah and London[69]	Developing laminar flow, rectangular	$Nu = 4.363 + 8.68(10^3x^*)^{-0.506}e^{-41x^*}$	$Nu = a + b(10^3x^*)^c e^{dx^*}$
Lee and Garimella [70]	Developing laminar flow, rectangular	$Nu = \frac{1}{C_1(x^*)^{C_2}+C_3} + C_4$ For $1 \leq \propto \leq 10, x < L_t$ $C_1 = P_3(\propto)$, $C_2 = const$ $C_3 = P_2(\propto)$, $C_4 = P_3(\propto)$	$Nu = \frac{1}{C_1(x^*)^{C_2}+C_3} + C_4$ For $1 \leq \propto \leq 10, x < L_t$ $C_{1,3,4} = P(\propto)$ $C_2 = const$

Experimental data for a number of frequencies and utilizations are used to fit the parameters in Eq. (13-14). In the friction factor fit, the oscillatory friction factor defined in Eq. (7) can be treated as temporal independent and can be fitted all through the experimental operating conditions. The *Nu* is sensitive to the fluid flowrate and therefore it is time dependent. Multi objective fitting as shown in Eq. (17) is implemented by using the numerical model to find the set of parameters that best matches the experimental temperature outlet curves to those predicted by the model:

$$\min_{c_3 > 0, c_4 \in R} (\boldsymbol{r}), \quad \boldsymbol{r} = \begin{bmatrix} r_1(c_3, c_4) \\ r_2(c_3, c_4) \\ r_3(c_3, c_4) \\ r_4(c_3, c_4) \end{bmatrix}, \begin{matrix} r_1 = \left\| \boldsymbol{T}_{f,c,model}(f_{min}, U_{min}) - \boldsymbol{T}_{f,c,exp}(f_{min}, U_{min}) \right\| \\ r_2 = \left\| \boldsymbol{T}_{f,c,model}(f_{max}, U_{min}) - \boldsymbol{T}_{f,c,exp}(f_{max}, U_{min}) \right\| \\ r_3 = \left\| \boldsymbol{T}_{f,c,model}(f_{min}, U_{max}) - \boldsymbol{T}_{f,c,exp}(f_{min}, U_{max}) \right\| \\ r_4 = \left\| \boldsymbol{T}_{f,c,model}(f_{max}, U_{max}) - \boldsymbol{T}_{f,c,exp}(f_{max}, U_{max}) \right\| \end{matrix} \quad (17)$$

where $\boldsymbol{r}$ is the residual tensor for least squares fitting. In detail, the magnitude of the residual, $\boldsymbol{r}$, is determined by the absolute value of difference between modelling and measurement values of $T_{\mathrm{f,h}}$ and $T_{\mathrm{f,c}}$ at 20 equidistant points for each blow. The condition of residual r_1 is derived from the case when the frequency and utilization are set at the minimum values within the operating range; while $r_2 \sim r_4$ correspond to other extreme cases for the variables frequency (f) and utilization (U). A nonlinear least-squares solver named lsqnonlin in MATLAB is applied to solve the parameters $c_3 \sim c_4$.

3.2.3. Model validation

Since new correlations are implemented, the parameters can be fitted with experiments. Neglecting the effect of fluid viscosity due to the temperature, c_1 and c_2 in Eq. (13) are fitted by pressure drop measurements. Based on the correctness of material properties, end temperature readings reflect the internal heat transfer conditions. Therefore the parameters c_3 and c_4 in Eq. (14) are fitted by $T_{\mathrm{f,h}}(t)$ and $T_{\mathrm{f,c}}(t)$ using the residual defined in Eq. (17). The modelling validation results with 20 experimental points in each curve are shown in Fig. 5 (a) and (b) for temperature and pressure drop respectively, for a number of different operating conditions. The model fits the overall behavior of the experiments without significant trend differences. In addition, the root mean square error (RMSE) in 84 operating conditions is summarized in Fig. 5 (c). Comparing the fit and experimental data, the deviation is < 0.5 ºC at temperature and < 0.02 bar at pressure drop, which indicates that the simulation results are in good agreement with the experimental readings, and thus that the model can be used to reveal the internal characteristics of a freeze-cast regenerator.

In order to reveal the sensitivity in terms of the heat transfer coefficient, Fig. 5 (d) presents the temperature responses of $T_{f,c}$ with the artificial perturbation of the heat transfer coefficient (scaling factor β) in the hot to cold blow. Since the errors of most correlations in the area of heat transfer are normally within 50%, perturbations of $0.5 < \beta < 1.5$ are adopted here to observe the system response. A perturbation in the decreasing direction ($\beta < 1$) is sensitive to temperature response, especially when $\beta < 0.8$. When the perturbation is in the increasing direction ($\beta > 1$), the scaling of the heat transfer coefficient is insensitive to temperature response, due to the small interface temperature differences. In this state, heat transfer performance is sufficient enough that over-scaling in heat transfer coefficient does not result in better performance significantly.

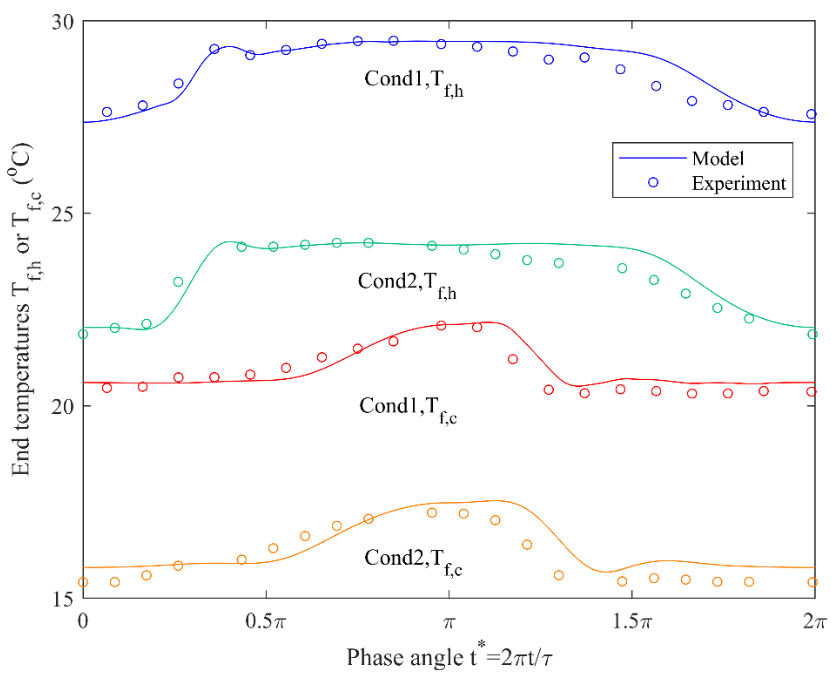

(a)

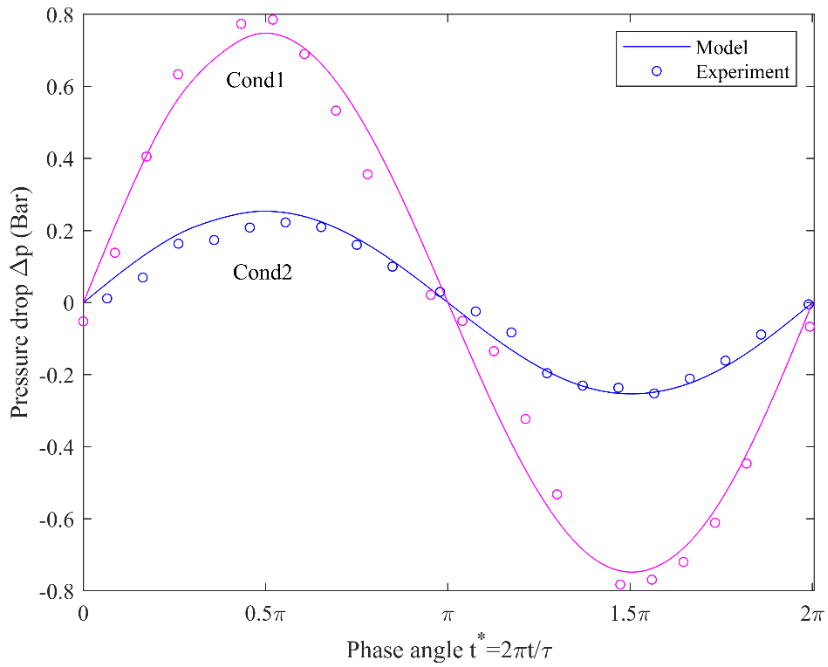
Model
Experiment
Cond1
Cond2
Pressure drop Δp (Bar)
Phase angle t*=2πt/τ
0.8
0.6
0.4
0.2
0
-0.2
-0.4
-0.6
-0.8
0
0.5π
π
1.5π
2π

(b)

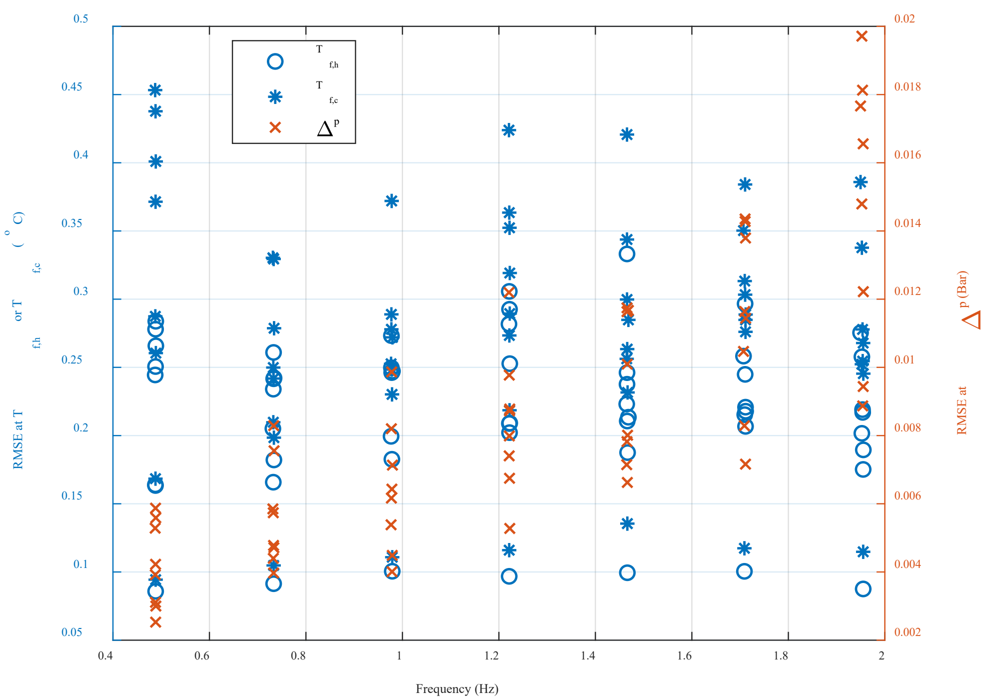
T f,h
T f,c
Δp
RMSE at T f,h or T f,c (°C)
RMSE at Δp (Bar)
Frequency (Hz)

(c)

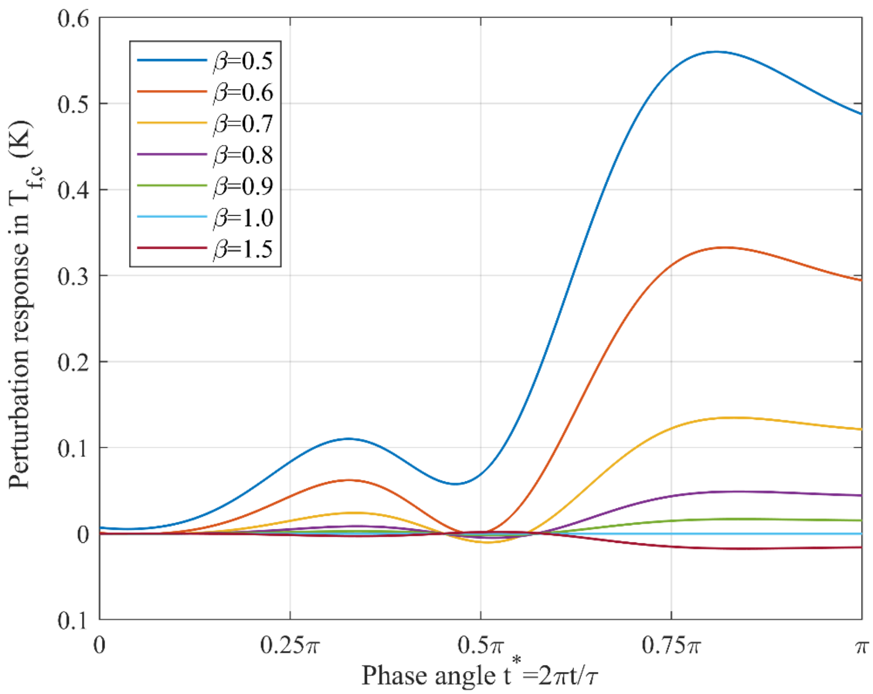

(d)

Fig. 5 Validations of (a) temperature and (b) pressure drop temporal evolution, Cond1 and Cond2 are different operating conditions corresponding to T_{c1} = 20 ºC, f_1 = 0.75 Hz and T_{c2}=15 ºC, f_2 = 2 Hz respectively. The model results are based on the fitted parameters c_1 - c_4. Figure (c) is the RMSE between the fit and experimental data under different frequencies. Figure (d) is the impact of heat transfer coefficient perturbation on the temperature profiles of cold end in the hot blow; y-axis is the temperature perturbation response of $T_{f,c}$ using $T_{f,c}(\beta = x) - T_{f,c}(\beta = 1)$, the legend is showing the value x of perturbation factors.

4. Results and discussions

The regenerator has been tested for nearly 700 hours in the passive experiment setup. It is noted that in the first sets of experiments, fine powder was observed coming out of the regenerator and was intercepted in the meshes. With the operation time increasing, the amount of powder coming out of the regenerator became less and less, until finally no powder could be seen with the naked eye. This illustrates both the somewhat brittle nature of LCSM materials but also the fact that residual “loose” material might be present within the freeze-cast structures after sintering.

4.1. Nusselt-Reynolds correlations

The overall spatial and temporal average Nusselt number ($\overline{Nu} = 1/L_r \int_0^{L_r}\left(1/\tau \int_0^{\tau} Nu(t,x)\,dt\right)dx$) is plotted as a function of cycle average $\overline{Re}_\mathrm{p}$ in Fig. 6. The local Nusselt number $Nu(t,x)$ varies due to variations in the local Reynolds number, which is caused by temperature and fluid velocity variations. In general, the trend of $Nu{\sim}Re$ is a sublinear relationship, which is similar to the cases of packed sphere beds [71], but different from the constant relationship in macro parallel plates [72]. For comparison, the fitted correlation for local Nu from Eq. (14) with c_3 = 0.34 and c_4 = -0.32 is plotted in the same figure. The correlation for local Re~Nu also fits the overall $\overline{Re}{\sim}\overline{Nu}$ trend well, which is convenient for overall evaluations of the freeze-cast regenerator. In comparison with the cases of the packed bed and rectangular micro-channel, also shown in Fig. 6, the absolute values of $\overline{Nu}$ for the freeze-cast regenerator are relatively lower than the packed bed one, but slightly higher than the rectangular micro-channel one. The main reasons for this are:

(1) Small hydraulic diameter: referring to the definition of Nu (Eq. (4)), a small hydraulic diameter results in a relatively small Nu value based on the same heat transfer coefficient. Recalling Table.1, the hydraulic diameter of the packed bed regenerator is significantly larger than that of the freeze-cast regenerator. In Fig. 6, the Nu in the packed bed regenerator outperforms that of the freeze-cast regenerator. Note that high Nu does not absolutely result in high heat transfer performance, because heat transfer area is another key factor.

(2) Limitation in oscillating blow evaluation: like single blow characterizations [73], temperature breakthroughs are insignificant when the interstitial temperature difference is tiny. In these situations, heat transfer enhancements only cause a slight change in temperature difference of solid-liquid, and therefore only small variations in temperature breakthroughs at the two ends of the regenerator. As illustrated in Fig. 5 (d), heat transfer coefficient is probably under-estimated due to this insensitivity.

(3) Different characterization methodologies: The Nu in the packed bed is from an ideal situation of steady state, no dead volume or maldistribution of the flow. In the case of rectangular micro channels in Fig. 6, the fit is from the steady state counterblow experiments without the effect of dead volume. For the characterization of a freeze-cast regenerator, factors of dead volume and uneven flow are unavoidably brought into the testing due to the nature of the passive rig. In principal, curves for Fig. 6 are not exactly in the same level of characterization. The values in the Nu fit on freeze-cast regenerator are further under-estimated due to these external influences.

According to the fit of Eq. (14), when Re_p approaches 0 in the limit, the Nu is unphysically approaching 0. However, in no-flow periods of (de)magnetization ($Re_\mathrm{p} = 0$) in AMR characterization, Nu should rather attain a positive value [74] considering the interstitial heat transfer via conduction. Thus, the fit extrapolated to near $Re_\mathrm{p} = 0$ may not be valid. The experimental Re_p in this study ranged from 1 to 15. Thus, the Nu fit in this paper is reasonably confined in the passive characterization within the operating range.

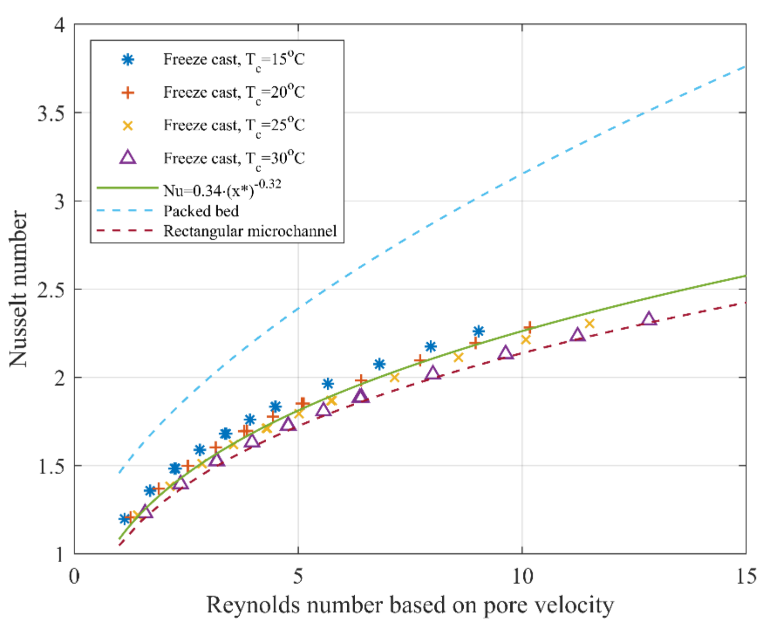

Fig.6 Nusselt number as a function of Reynolds number. The markers are $(\overline{Re}_{\mathrm{p}}, \overline{Nu})$ from the numerical model with fitted correlations under different operations. The plotting of packed bed is taken from the correlations of Ref. [71] with the same parameters as the reference Gd regenerator. The fit of rectangular micro-channel heat exchanger is taken from Ref. [60] based on the counterblow experiment of steady state. The width and depth of the rectangular micro channels are 0.2 mm and 0.6 mm, respectively.

4.2. Friction factor correlations

The behavior of f_{F}~Re is depicted in Fig. 7 at different operating conditions. The absolute values of f are relatively high due to the small hydraulic diameter. The general trend of the f_{F}~Re relationship collapses into one single curve. These relations are picked up by model fitting from Eq. (13) (c_1 = 358.8 and c_2 = 0.3951) and also fit the form of the Ergun equation ([75], rewritten in Eq.(18)). The model profiles are in qualitative agreement with the experimental behavior. The physical relations of $f_F \sim Re$ from packed beds are still suitable for freeze-cast regenerators with different regression parameters.

$$f_F = \frac{1}{4} f_D = \frac{1}{4}\left[\underbrace{\beta_1 \frac{(1-\varepsilon)^2}{\varepsilon^4} \cdot \left(\frac{6D_h}{D_{sp}}\right)^2}_{\mathrm{c_1\ regression}} \cdot Re_p^{-1} + \underbrace{\beta_2 \frac{1-\varepsilon}{16\varepsilon^3} \cdot \left(\frac{6D_h}{D_{sp}}\right)}_{\mathrm{c_2\ regression}}\right] \quad (18)$$

where f_{D} is Darcy friction factor, D_{sp} is the particle diameter and $\beta_1 \approx 2.5$ and $\beta_2 = 2.4$ in Ref.[75].

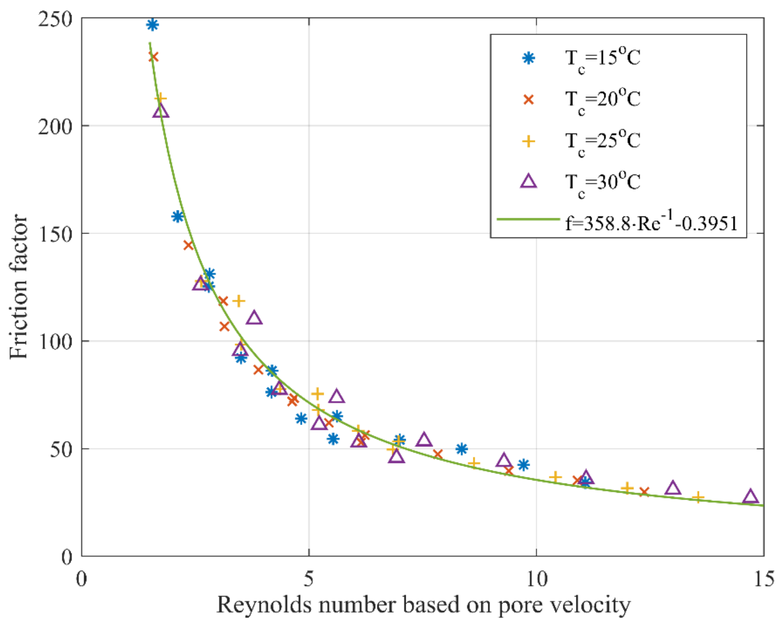

Fig.7 Experimental friction factor as a function of Reynolds number under different conditions for the freeze-cast regenerator.

4.3. Heat transfer versus flow resistance

To evaluate the whole regenerator, the curves of $\eta \sim (U, \mathrm{NTU})$ are presented in Fig. 8 for both the freeze-cast regenerator and the baseline Gd packed sphere regenerator. Theoretically, the regenerator can only reach the ideal 100% effectiveness when the utilization is lower than or equal to unity. Considering the limitations of the discrete numbers in piston stroke and piston seal capacity at high frequencies, the utilization of the Gd regenerator is set at ~0.59, compared to the value of 0.67 in the freeze-cast regenerator.

Based on the fixed utilization and housing size but different T_c in the freeze-cast regenerator, the experiments lead to different η~NTU curves. The reasons are attributed to the loss differences between the different regenerators, as well as the impact of temperature dependent properties of the regenerator material (Fig. 4). In general, the effectiveness is observed to increase with NTU. Note that within the operating conditions' range, increasing the operating frequency decreases the NTU. The reason can be identified from the definition in Eq. (3); the fluid thermal mass increments are more significant than the heat transfer coefficient enhancement. In some utilization regions, the effectiveness is decreasing with increasing NTU. From our extra testing in this passive rig, and combined with previous work [76], we summarize the reasons of this decreasing trend as: (1) Trade-off between heat transfer improving rate and heat transfer cycle time; (2) Axial heat conduction when operating at low utilization; (3) Dead void effect, especially in high NTU (low frequency); and (4) Equipment problems, such as the piston working at high frequency (low NTU) and long stroke (high utilization) would breathe in some air, reducing the local utilization or causing some miscalculation due to the out-of-phase of $T_{f,h}$ and $T_{f,c}$. The values of effectiveness of the Gd and freeze-cast regenerators are compared at T_c = 30 °C to ensure the temperature is far away from the peak value of the specific heat in both LCSM and Gd. Although the Gd regenerator has the advantage of ~10% lower value of utilization than the freeze-cast regenerator, the absolute values of effectiveness in the freeze-cast regenerator are still slightly higher than the Gd one on average (0.942 compared to 0.935). NTU in the freeze-cast regenerator is also higher than for the Gd regenerator. That means that the freeze-cast regenerator shows excellent heat transfer performance.

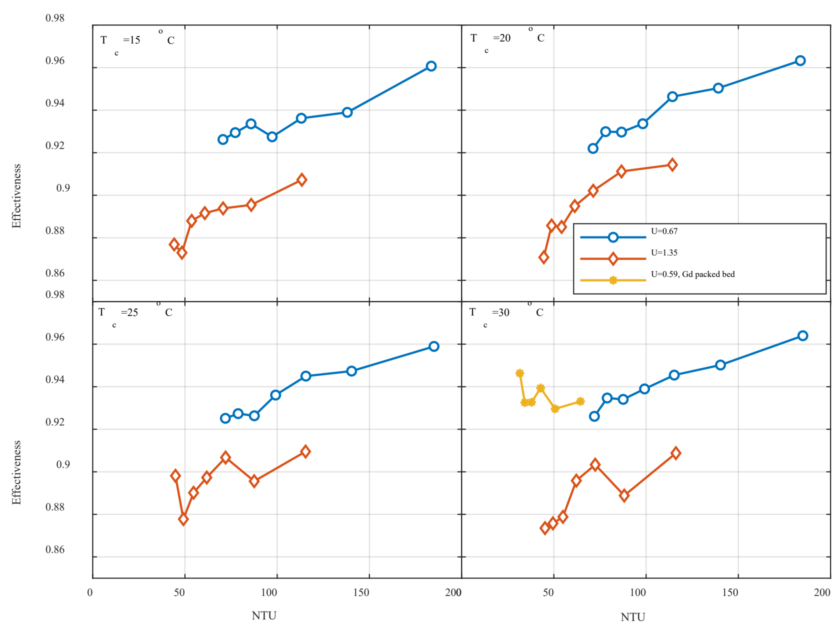

Fig.8 Effectiveness curves for freeze-cast regenerator and baseline regenerator.

Regarding the utilization impact, most regenerators follow the conventional behaviors that effectiveness increases when the utilization decreases. High effectiveness requires a small difference of regenerator temperature profile between hot blow and cold blow, which indicates a small utilization with lower penetration of inflow fluid into the material matrix. In Fig. 9, we compare the effectiveness versus the utilization among different regenerators. In this dimension, the freeze-cast regenerator also has the best value of effectiveness among other regenerators.

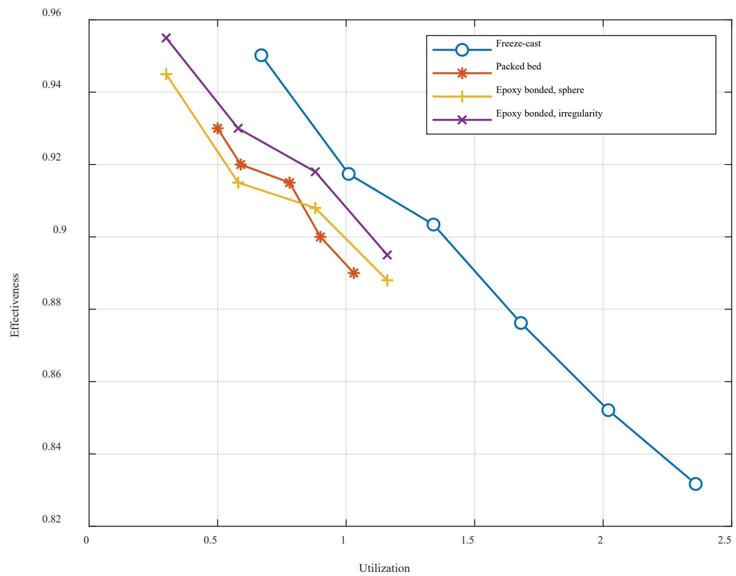

Fig.9 Effectiveness comparison for the freeze-cast regenerator, Gd packed bed regenerator and epoxy bonded regenerators with spherical and irregular particles. All the regenerators operate at the frequency of 1Hz. The cold reservoir temperatures are set to 30 ºC for packed bed and freeze-cast regenerators and 22-24 ºC for epoxy bonded regenerators, which are all above the Curie temperature.

As a preliminary test for the freeze-cast regenerator, it is valuable to provide the data of pressure drop and compare them to other reference regenerators in Table 1 tested in the same tester. Despite the fact that regenerators with different hydraulic diameters result in various values of pressure drop, the pressure drop data for freeze-cast regenerators can give a rough comparison of pumping work for further investigation. From Fig.A1, the pressure drop signal is approximately a sinusoidal waveform. The minor deviations are probably caused by the check valves' response, inertial velocity and sensor fluctuations. More important concerns are the relation of maximum pressure drop and pore velocity under different conditions. We compare the viscous dissipation effect of the freeze-cast regenerator and other regenerators by using the curve of pressure drop versus pore velocity in Fig. 10. From the curve the trend of the freeze-cast regenerator is captured as a nearly linear behavior, which is similar to the parallel plate regenerators [76]. In this case, most of the working conditions are in the Darcy regime. The variations are mainly caused by the temperature dependence of the fluid viscosity. Higher temperature values result in a relatively lower pressure drop. On the other hand, the absolute values of pressure drop in the freeze-cast regenerator are larger than in the Gd packed bed and epoxy bonded regenerators with spherical particles, because of the small hydraulic diameter. In the case of the epoxy bonded regenerator with irregular particles, its curve is close to that of the freeze-cast regenerator. However, the housings in the epoxy bonded regenerators are thinner and longer than in the freeze-cast and Gd packed bed regenerators, which is shown in Table 1. Consequently, the measured pressure drop in the freeze-cast regenerator is larger than in epoxy bonded and Gd packed bed regenerators based on the similar housing.

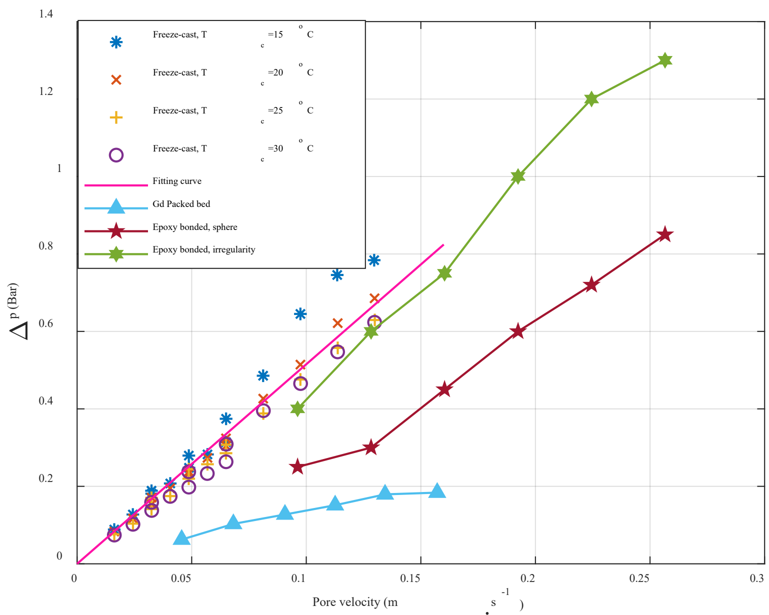

Fig.10 Comparison of pressure drop versus pore velocity among freeze-cast regenerator, Gd packed bed regenerator and epoxy bonded regenerators with irregular and spherical particles.

In order to connect heat transfer and flow resistance and highlight the characteristics of the target regenerator, the data of *UA* (heat transfer coefficient times heat transfer area) versus pressure drop between the freeze-cast regenerator and the baseline Gd packed bed regenerator are plotted in Fig. 11. It should be noted that adopting *UA* as a representative of heat transfer performance is due to its small error as well as including not only values of *Nu* but also the surface area of the regenerator. From the general heat transfer rate equation of $\dot{Q} = UA\,\Delta T$, the total heat transfer area *A* is obtained from the image analysis mentioned previously with unquantified error. However, the terms of $\dot{Q}$ and ΔT are derived indirectly from temperature data through the numerical modelling. Since the errors of modelling and temperature measurements are validated to be small, the errors of $\dot{Q}$, ΔT and therefore the *UA*, can be treated as being small. In general, *UA* increases with the pressure drop. Some variations are captured based on the same Δp, because different working temperatures result in a variation of viscosity values and therefore different values of Re_p. The freeze-cast regenerator exhibits higher values of heat transfer performance for a given pressure drop compared to the packed Gd sphere regenerator. The main contributions are large specific area and small hydraulic diameter. When fixing the pressure drop, the value of *UA* in the freeze-cast regenerator is approximate 10-15% higher than that in Gd regenerator. Based on existing features, this regenerator is more suitable for running in the situations of low flowrate and high performance requirements. On the other hand, it is necessary to develop variable freeze-cast regenerators that fit in different flow conditions. For instance, freeze-cast regenerators with large pore size and porosity may exhibit relatively low flow resistance.

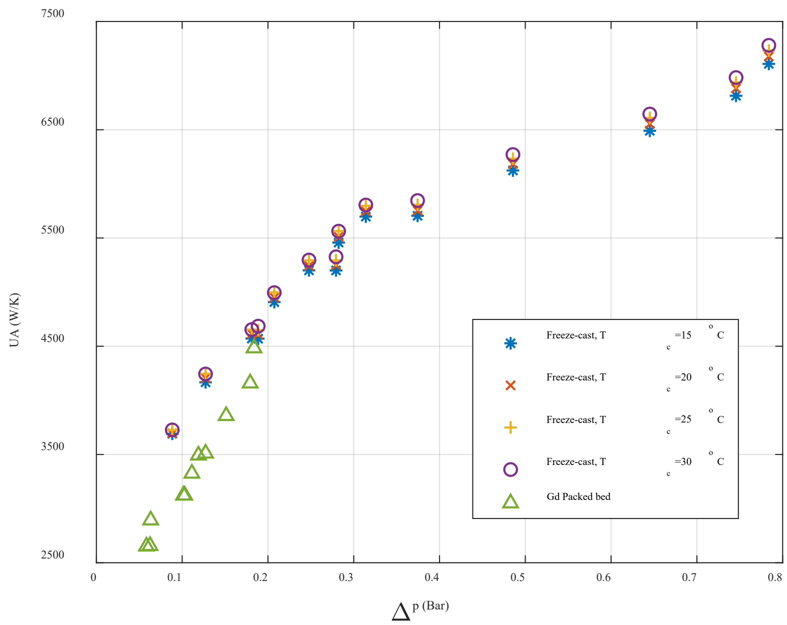

Fig.11 *UA* and pressure drop between freeze-cast and Gd packed bed regenerators.

5. Conclusion

In this study, a novel type of regenerator fabricated by the technique of freeze-casting was thermally and hydraulically characterized. A passive test rig was used to obtain the effectiveness and friction factor, as well as the modelling correlation validations of heat and mass transfer. Numerical analysis was performed to reveal the in-depth thermodynamic parameters of NTU and heat transfer coefficients. The following features are obtained due to the thermal evaluations:

(1) The overall Nusselt number matches the local fitted Nusselt number correlation well, and the increasing trend with Reynolds number is sublinear. The absolute value of the Nusselt number is relatively low due to the small hydraulic diameter, limitation of oscillating blow evaluation and external thermal loss interference.
(2) The relationship of friction factor and Reynolds number fit in the Ergun equation form, but with different regression parameter values.
(3) The freeze-cast regenerator has both higher effectiveness and pressure drop than in the packed gadolinium sphere bed and epoxy bonded regenerators.
(4) The pressure drop shows a nearly linear behavior due to the low Reynolds numbers. The curve trend is fitting in the situation of Darcy regime.
(5) The combined characteristics of heat transfer performance and flow resistance of the freeze-cast regenerator are high. When the pressure drop is held constant, the *UA* values for the freeze-cast regenerators are 10-15% higher than the values in the packed bed regenerator. Further, the pore size and porosity could be tunable within certain range for different potential applications.

The characterization and modelling correlations are only based on the current pore size and tortuosity of the sample. Sensitivity studies on the parameters of hydraulic diameter, porosity and channel tortuosity, as well as the parametric passive and active characterizations, will be covered in future work.

Acknowledgments

J. Liang is grateful for financial support of the CSC (China Scholarship Council) scholarship. C. D. Christiansen, R. Bjørk and K. K. Nielsen wish to acknowledge the financial support of the Independent Research Fund Denmark—Technologies and Productions Sciences, project no. 6111 - 00073B.

Appendix A: Uncertainty analysis

To carry out uncertainty analysis, temperature and pressure measurements are regarded as observations here and designated as X. Extensive repeatability cycles are performed to validate the experimental procedure. To correct the reading oscillations, average treatments between cycles are taken into the data reduction for deriving the mean values:

$$\bar{X}(t) = \frac{1}{n}\sum_{i=0}^{n} X(t + i \cdot \tau),\ \ X = T_h,\ T_c, T_{f,h}, T_{f,c}, p_1, p_2 \qquad \text{(A.1)}$$

Where repeatability number $\mathrm{n} = 20$; t and τ represent the time readings and cycle period, respectively. For small sets of data, the standard deviation of repeatability is defined by averaging the cycle deviations [77]:

$$\sigma_1(t) = \sqrt{\sum_{\mathrm{i}=1}^{\mathrm{n}}\left(X(t + i \cdot \tau) - \bar{X}(t)\right)^2/(n-1)} \qquad \text{(A.2)}$$

Assuming the measurement uncertainties are only due to issues with the repeatability, the overall standard deviation is written from the error propagation principle:

$$\sigma(t) = \sqrt{\sigma_1^2(t) + \sigma_2^2(t)} \qquad \text{(A.3)}$$

Where $\sigma_2(t)$ is the instrument deviation based on current local temperature of 0.5% and pressure of 0.25%. We extract four cycles of temperature and pressure measurements with 95% confidence level region $X \pm 2\sigma$ in Fig.A1. Less than 3% uncertainties are obtained from both temperature and pressure measurements.

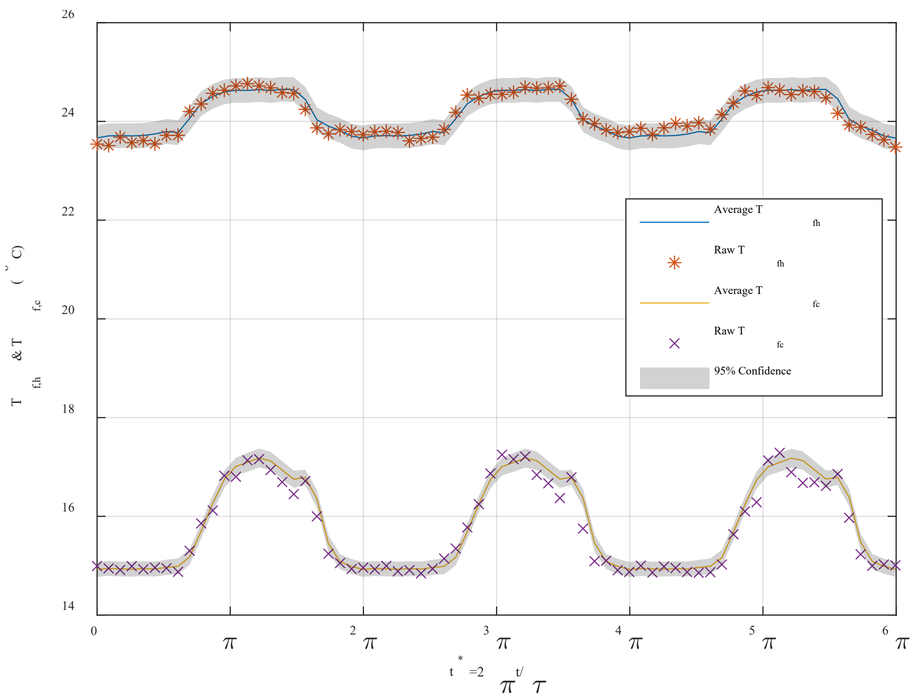

(a)

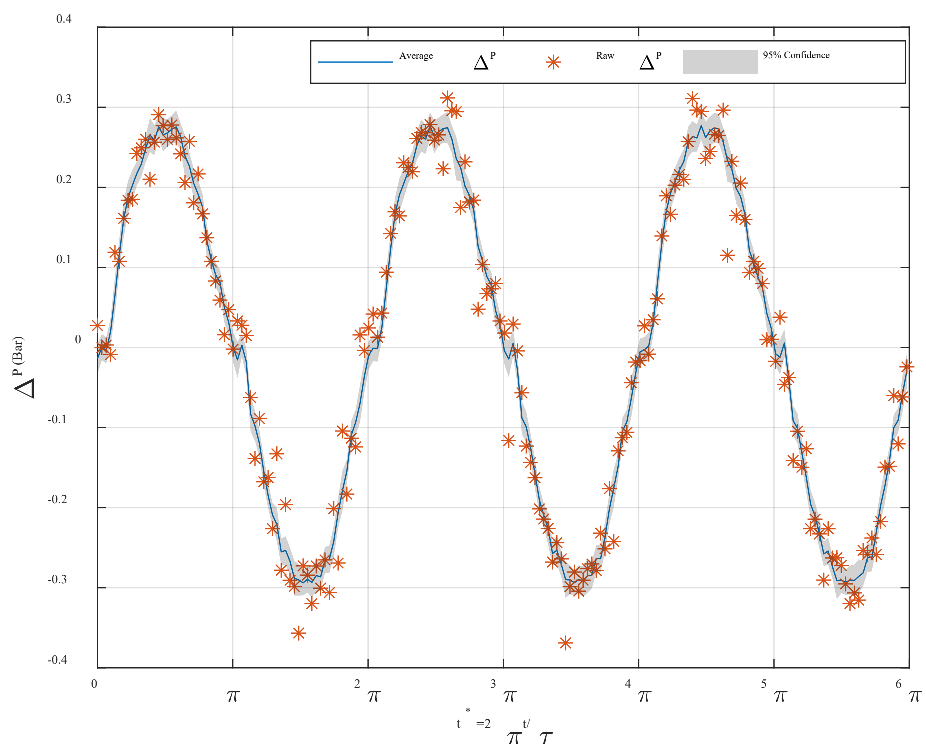

(b)

Fig.A1 Temperature (a) and pressure drop (b) measurements of a single operating condition compared with the average data over 20 cycles

References

[1] V. Franco, J.S. Blázquez, J.J. Ipus, J.Y. Law, L.M. Moreno-Ramírez, A. Conde, Magnetocaloric effect: From materials research to refrigeration devices, Prog. Mater. Sci. 93 (2018) 112–232. doi:10.1016/j.pmatsci.2017.10.005.

[2] A. Kitanovski, Energy Applications of Magnetocaloric Materials, Adv. Energy Mater. 1903741 (2020) 1903741. doi:10.1002/aenm.201903741.

[3] V. Chaudhary, X. Chen, R. V. Ramanujan, Iron and manganese based magnetocaloric materials for near room temperature thermal management, Prog. Mater. Sci. 100 (2019) 64–98. doi:10.1016/j.pmatsci.2018.09.005.

[4] K. Klinar, U. Tomc, B. Jelenc, S. Nosan, A. Kitanovski, New frontiers in magnetic refrigeration with high oscillation energy-efficient electromagnets, Appl. Energy. 236 (2019) 1062–1077. doi:10.1016/j.apenergy.2018.12.055.

[5] F.P. Fortkamp, J.A. Lozano, J.R. Barbosa, Analytical solution of concentric two-pole Halbach cylinders as a preliminary design tool for magnetic refrigeration systems, J. Magn. Magn. Mater. 444 (2017) 87–97. doi:10.1016/j.jmmm.2017.07.072.

[6] J. Lee, J. Lee, Magnetic force enhancement using air-gap magnetic field manipulation by optimized coil currents, Appl. Sci. 10 (2020). doi:10.3390/app10010104.

[7] T. Lei, K. Engelbrecht, K.K. Nielsen, C.T. Veje, Study of geometries of active magnetic regenerators for room temperature magnetocaloric refrigeration, Appl. Therm. Eng. 111 (2017) 1232–1243. doi:10.1016/j.applthermaleng.2015.11.113.

[8] A. Czernuszewicz, J. Kaleta, D. Kołosowski, D. Lewandowski, Experimental study of the effect of regenerator bed length on the performance of a magnetic cooling system, Int. J. Refrig. 97 (2019) 49–55. doi:10.1016/j.ijrefrig.2018.09.023.

[9] P. V. Trevizoli, R. Teyber, P.S. da Silveira, F. Scharf, S.M. Schillo, I. Niknia, P. Govindappa, T. V. Christiaanse, A. Rowe, Thermal-hydraulic evaluation of 3D printed microstructures, Appl. Therm. Eng. 160 (2019) 113990. doi:10.1016/j.applthermaleng.2019.113990.

[10] A. Smith, Who discovered the magnetocaloric effect? Warburg, Weiss, and the connection between magnetism and heat, Eur. Phys. J. H. (2013). doi:10.1140/epjh/e2013-40001-9.

[11] V.K. Pecharsky, K.A. Gschneidner, Magnetocaloric effect and magnetic refrigeration, J. Magn. Magn. Mater. (1999). doi:10.1016/S0304-8853(99)00397-2.

[12] V. Basso, M. Küpferling, C. Curcio, C. Bennati, A. Barzca, M. Katter, M. Bratko, E. Lovell, J. Turcaud, L.F. Cohen, Specific heat and entropy change at the first order phase transition of La(Fe-Mn-Si)13H compounds, J. Appl. Phys. 118 (2015). doi:10.1063/1.4928086.

[13] A.R. Dinesen, S. Linderoth, S. Mørup, Direct and indirect measurement of the magnetocaloric effect in La0.67Ca0.33-xSrxMnO3 ± δ(x ∈ [0;0.33]), J. Phys. Condens. Matter. 17 (2005) 6257–6269. doi:10.1088/0953-8984/17/39/011.

[14] V.K. Pecharsky, K.A. Gschneidner, Giant magnetocaloric effect in Gd5 (Si2 Ge2), Phys. Rev. Lett. (1997). doi:10.1103/PhysRevLett.78.4494.

[15] A. Gschneidner, V.K. Pecharsky, A.O. Tsokol, Recent developments in magnetocaloric materials, Reports Prog. Phys. 68 (2005) 1479–1539. doi:10.1088/0034-4885/68/6/R04.

[16] E. Brück, O. Tegus, D.T.C. Thanh, K.H.J. Buschow, Magnetocaloric refrigeration near room temperature (invited), J. Magn. Magn. Mater. (2007). doi:10.1016/j.jmmm.2006.10.1146.

[17] S.Y. Dan'kov, A. Tishin, V. Pecharsky, K. Gschneidner, Magnetic phase transitions and the magnetothermal properties of gadolinium, Phys. Rev. B - Condens. Matter Mater. Phys. (1998). doi:10.1103/PhysRevB.57.3478.

[18] R. Bjørk, C.R.H. Bahl, M. Katter, Magnetocaloric properties of LaFe13-x-yCoxSi y and commercial grade Gd, J. Magn. Magn. Mater. (2010). doi:10.1016/j.jmmm.2010.08.013.

[19] A. Kitanovski, U. Plaznik, J. Tušek, A. Poredoš, New thermodynamic cycles for magnetic refrigeration, Int. J. Refrig. 37 (2014) 28–35. doi:10.1016/j.ijrefrig.2013.05.014.

[20] J. Romero Gómez, R. Ferreiro Garcia, A. De Miguel Catoira, M. Romero Gómez, Magnetocaloric effect: A review of the thermodynamic cycles in magnetic refrigeration, Renew. Sustain. Energy Rev. 17 (2013) 74–82.

doi:10.1016/j.rser.2012.09.027.

[21] Z. Li, J. Shen, K. Li, X. Gao, X. Guo, W. Dai, Assessment of three different gadolinium-based regenerators in a rotary-type magnetic refrigerator, Appl. Therm. Eng. 153 (2019) 159–167. doi:10.1016/j.applthermaleng.2019.02.100.

[22] F.P. Fortkamp, D. Eriksen, K. Engelbrecht, C.R.H. Bahl, J.A. Lozano, J.R. Barbosa, Experimental investigation of different fluid flow profiles in a rotary multi-bed active magnetic regenerator device, Int. J. Refrig. 91 (2018) 46–54. doi:10.1016/j.ijrefrig.2018.04.019.

[23] A.T.D. Nakashima, S.L. Dutra, P. V. Trevizoli, J.R. Barbosa, Influence of the flow rate waveform and mass imbalance on the performance of active magnetic regenerators. Part I: Experimental analysis, Int. J. Refrig. 93 (2018) 236–248. doi:10.1016/j.ijrefrig.2018.07.004.

[24] A.T.D. Nakashima, S.L. Dutra, P. V. Trevizoli, J.R. Barbosa, Influence of the flow rate waveform and mass imbalance on the performance of active magnetic regenerators. Part II: Numerical simulation, Int. J. Refrig. 93 (2018) 159–168. doi:10.1016/j.ijrefrig.2018.07.005.

[25] R. Teyber, P. V. Trevizoli, I. Niknia, T. V. Christiaanse, P. Govindappa, A. Rowe, Experimental performance investigation of an active magnetic regenerator subject to different fluid flow waveforms, Int. J. Refrig. 74 (2017) 36–44. doi:10.1016/j.ijrefrig.2016.10.001.

[26] K. Navickaitė, H.N. Bez, T. Lei, A. Barcza, H. Vieyra, C.R.H. Bahl, K. Engelbrecht, Experimental and numerical comparison of multi-layered La(Fe,Si,Mn)13Hy active magnetic regenerators, Int. J. Refrig. 86 (2018) 322–330. doi:10.1016/j.ijrefrig.2017.10.032.

[27] P. V. Trevizoli, A.T. Nakashima, G.F. Peixer, J.R. Barbosa, Performance evaluation of an active magnetic regenerator for cooling applications – part I: Experimental analysis and thermodynamic performance, Int. J. Refrig. 72 (2016) 192–205. doi:10.1016/j.ijrefrig.2016.07.009.

[28] A. Kitanovski, J. Tušek, U. Tomc, U. Plaznik, M. Ožbolt, A. Poredoš, Magnetocaloric Energy Conversion: From Theory to Applications, 2015. doi:10.1007/978-3-319-08741-2.

[29] A. Greco, C. Aprea, A. Maiorino, C. Masselli, A review of the state of the art of solid-state caloric cooling processes at room-temperature before 2019, Int. J. Refrig. 106 (2019) 66–88. doi:10.1016/j.ijrefrig.2019.06.034.

[30] T. Lei, K. Navickaitė, K. Engelbrecht, A. Barcza, H. Vieyra, K.K. Nielsen, C.R.H. Bahl, Passive characterization and active testing of epoxy bonded regenerators for room temperature magnetic refrigeration, Appl. Therm. Eng. 128 (2018) 10–19. doi:10.1016/j.applthermaleng.2017.08.152.

[31] P. V. Trevizoli, G.F. Peixer, J.R. Barbosa, Thermal-hydraulic evaluation of oscillating-flow regenerators using water: Experimental analysis of packed beds of spheres, Int. J. Heat Mass Transf. 99 (2016) 918–930. doi:10.1016/j.ijheatmasstransfer.2016.03.014.

[32] A. Šarlah, J. Tušek, A. Poredoš, Comparison of thermo-hydraulic properties of heat regenerators applicable to active magnetic refrigerators, Stroj. Vestnik/Journal Mech. Eng. 58 (2012) 16–22. doi:10.5545/sv-jme.2010.250.

[33] A.A. Boroujerdi, M. Esmaeili, Characterization of the frictional losses and heat transfer of oscillatory viscous flow through wire-mesh regenerators, Alexandria Eng. J. 54 (2015) 787–794. doi:10.1016/j.aej.2015.06.001.

[34] P. Li, M. Gong, J. Wu, Geometric optimization of an active magnetic regenerative refrigerator via second-law analysis, J. Appl. Phys. 104 (2008). doi:10.1063/1.3032195.

[35] K.K. Nielsen, K. Engelbrecht, C.R.H. Bahl, The influence of flow maldistribution on the performance of inhomogeneous parallel plate heat exchangers, Int. J. Heat Mass Transf. 60 (2013) 432–439. doi:10.1016/j.ijheatmasstransfer.2013.01.018.

[36] J.D. Moore, D. Klemm, D. Lindackers, S. Grasemann, R. Träger, J. Eckert, L. Löber, S. Scudino, M. Katter, A. Barcza, K.P. Skokov, O. Gutfleisch, Selective laser melting of La(Fe,Co,Si)13geometries for magnetic refrigeration, J. Appl. Phys. 114 (2013). doi:10.1063/1.4816465.

[37] T. Lei, K. Engelbrecht, K.K. Nielsen, C.T. Veje, J. Tušek, C.R.H. Bahl, Modelling and comparison studies of packed screen regenerators for active magnetocaloric refrigeration, in: Proceedings of the 6th IIF-IIR international Conference on Magnetic Refrigeration, 2014.

[38] R. Radebaugh, B. Louie, Simple, First Step To the Optimization of Regenerator Geometry., in: Natl. Bur. Stand. Spec. Publ., 1985.

[39] J. Li, T. Numazawa, K. Matsumoto, Y. Yanagisawa, H. Nakagome, A modeling study on the geometry of active magnetic regenerator, in: AIP Conf. Proc., 2012: pp. 327–334. doi:10.1063/1.4706936.

[40] S. Deville, E. Saiz, A.P. Tomsia, Ice-templated porous alumina structures, Acta Mater. (2007). doi:10.1016/j.actamat.2006.11.003.

[41] T. Waschkies, R. Oberacker, M.J. Hoffmann, Control of lamellae spacing during freeze casting of ceramics using double-side cooling as a novel processing route, in: J. Am. Ceram. Soc., 2009. doi:10.1111/j.1551-2916.2008.02673.x.

[42] A.Z. Lichtner, D. Jauffrès, C.L. Martin, R.K. Bordia, Processing of hierarchical and anisotropic porosity LSM-YSZ composites, J. Am. Ceram. Soc. (2013). doi:10.1111/jace.12478.

[43] S. Deville, The lure of ice-templating: Recent trends and opportunities for porous materials, Scr. Mater. (2018). doi:10.1016/j.scriptamat.2017.06.020.

[44] B.S. Deville, Freeze-Casting of Porous Ceramics : A Review of Current Achievements, (2008) 155–169. doi:10.1002/adem.200700270.

[45] C.D. Christiansen, K.K. Nielsen, R.K. Bordia, R. Bjørk, The effect of gelation on statically and dynamically freeze-cast structures, J. Am. Ceram. Soc. (2019). doi:10.1111/jace.16500.

[46] W.M. Kays, M.E. Crawford, Convecitve Heat and Mass Transfer, McGraw-Hill, Inc., 1993.

[47] S.G. Kandlikar, S. Garimella, D. Li, S. Colin, M. King, Heat Transfer and Fluid Flow in Minichannels and Microchannels, 2013. doi:10.1016/C2011-0-07521-X.

[48] T. Lei, Modeling of active magnetic regenerators and experimental investigation of passive regenerators with oscillating flow, Technical University of Denmark, 2016.

[49] C.D. Christiansen, K.K. Nielsen, R. Bjørk, Freeze-casting to create create directional micro-channels in regenerators for magnetic refrigeration, Proc. TherMag VIII, 8th IIF-IIR Int. Conf. Caloric Cool. (2018) 96–101. doi:10.18462/iir.11072.

[50] A. Bareggi, E. Maire, A. Lasalle, S. Deville, Dynamics of the freezing front during the solidification of a colloidal alumina aqueous suspension: In situ x-ray radiography, tomography, and modeling, J. Am. Ceram. Soc. (2011). doi:10.1111/j.1551-2916.2011.04572.x.

[51] S. Deville, E. Maire, A. Lasalle, A. Bogner, C. Gauthier, J. Leloup, C. Guizard, In situ X-ray radiography and tomography observations of the solidification of aqueous alumina particle suspensions - Part I: Initial instants, J. Am. Ceram. Soc. (2009). doi:10.1111/j.1551-2916.2009.03163.x.

[52] S. Choi, K. Nam, S. Jeong, Investigation on the pressure drop characteristics of cryocooler regenerators under oscillating flow and pulsating pressure conditions, Cryogenics (Guildf). 44 (2004) 203–210. doi:10.1016/j.cryogenics.2003.11.006.

[53] T.S. Zhao, P. Cheng, Oscillatory pressure drops through a woven-screen packed column subjected to a cyclic flow, Cryogenics (Guildf). 36 (1996) 333–341. doi:10.1016/0011-2275(96)81103-9.

[54] K. Nam, S. Jeong, Novel flow analysis of regenerator under oscillating flow with pulsating pressure, Cryogenics (Guildf). 45 (2005) 368–379. doi:10.1016/j.cryogenics.2005.01.001.

[55] F. Mohd Saat, A. Jaworski, Friction Factor Correlation for Regenerator Working in a Travelling-Wave Thermoacoustic System, Appl. Sci. 7 (2017) 253. doi:10.3390/app7030253.

[56] Y. Ju, Y. Jiang, Y. Zhou, Experimental study of the oscillating flow characteristics for a regenerator in a pulse tube cryocooler, Cryogenics (Guildf). 38 (1998) 649–656. doi:10.1016/S0011-2275(98)00037-X.

[57] K. Engelbrecht, C.R.H. Bahl, Evaluating the effect of magnetocaloric properties on magnetic refrigeration performance, J. Appl. Phys. (2010). doi:10.1063/1.3525647.

[58] I.H. Bell, J. Wronski, S. Quoilin, V. Lemort, Pure and pseudo-pure fluid thermophysical property evaluation and the open-source thermophysical property library coolprop, Ind. Eng. Chem. Res. (2014). doi:10.1021/ie4033999.

[59] K.K. Nielsen, A. Smith, C.R.H. Bahl, U.L. Olsen, The influence of demagnetizing effects on the performance of active magnetic regenerators, J. Appl. Phys. 112 (2012). doi:10.1063/1.4764039.

[60] P. Jiang, M. Fan, G. Si, Z. Ren, Thermal-hydraulic performance of small scale micro-channel and porous-media heat exchangers, Int. J. Heat Mass Transf. 44 (2001).

[61] F.S. Shih, Laminar flow in axisymmetric conduits by a rational approach, Can. J. Chem. Eng. 45 (1967) 285–294. doi:10.1002/cjce.5450450507.

[62] R.W. Hornbeck, Laminar flow in the entrance region of a pipe, Appl. Sci. Res. (1964). doi:10.1007/BF00382049.

[63] M.E. Steinke, Single-Phase Liquid Heat Transfer in Microchannels, Int. Conf. Microchannels Minichannels. (2005) 1–12. doi:10.1115/ICNMM2006-96227.

[64] M. Lorenzini, G. Morini, Poiseuille and Nusselt numbers for laminar flow in microchannels with rounded corners, in: 2nd Micro Nano Flows Conf., West London, 2009. http://dspace.brunel.ac.uk/handle/2438/6936.

[65] T.M. Liou, C.S. Wang, H. Wang, Nusselt number and friction factor correlations for laminar flow in parallelogram serpentine micro heat exchangers, Appl. Therm. Eng. 143 (2018) 871–882. doi:10.1016/j.applthermaleng.2018.08.021.

[66] S.B. Choi, R.F. Barron, R.O. Warrington, Fluid flow and heat transfer in microtubes, Am. Soc. Mech. Eng. Dyn. Syst. Control Div. DSC. 32 (1991) 123–134.

[67] Helmuth Hausen, Heat Transfer in Counterflow Parallel Flow And Cross Flow, 1983.

[68] E. Sadeghi, M. Bahrami, N. Djilali, Estimation of nusselt number in microchannels of arbitrary cross section with constant axial heat flux, Heat Transf. Eng. 31 (2010) 666–674. doi:10.1080/01457630903466647.

[69] R.K. Shah, A.L. London, Laminar Flow Forced Convection in Ducts, 1978. doi:10.1016/B978-0-12-020051-1.50022-X.

[70] P.S. Lee, S. V. Garimella, Thermally developing flow and heat transfer in rectangular microchannels of different aspect ratios, Int. J. Heat Mass Transf. 49 (2006) 3060–3067. doi:10.1016/j.ijheatmasstransfer.2006.02.011.

[71] K. Engelbrecht, A Numerical Model of an Active Magnetic Regenerator Refrigerator with Experimental Validation, University of Wisconsin-Madison, 2008.

[72] M. Nickolay, H. Martin, Improved approximation for the Nusselt number for hydrodynamically developed laminar flow between parallel plates, Int. J. Heat Mass Transf. 45 (2002) 3263–3266. doi:10.1016/S0017-9310(02)00028-5.

[73] P.J. Heggs, D. Burns, Single-blow experimental prediction of heat transfer coefficients. A comparison of four commonly used techniques, Exp. Therm. Fluid Sci. (1988). doi:10.1016/0894-1777(88)90003-9.

[74] K.K. Nielsen, G.F. Nellis, S.A. Klein, Numerical modeling of the impact of regenerator housing on the determination of Nusselt numbers, Int. J. Heat Mass Transf. 65 (2013) 552–560. doi:10.1016/j.ijheatmasstransfer.2013.06.032.

[75] S. Ergun, A.A. Orning, Fluid Flow through Randomly Packed Columns and Fluidized Beds, Ind. Eng. Chem. 41 (1949) 1179–1184. doi:10.1021/ie50474a011.

[76] Paulo Vinicius Trevizoli, Development of thermal regenerators for magnetic cooling applications, Federal University of Santa Catarina, 2015.

[77] J.P. Holman, Experimental Methods for Engineers, Eighth Edi, The McGraw-Hill companies, 2011.